Influence of the Vibrational Modes from the Organic Moieties in Two-Dimensional Lead Halides on Excitonic Recombination and Phase Transition

[1]Raphael F. Moral, [1]José C. Germino, [1]Luiz G. Bonato, [2]Diogo B. Almeida, [1,3]Eralci M. Therézio, [1]Teresa D. Z. Atvars, [4,5]Samuel D. Stranks, [1]René A. Nome, and [1]Ana F. Nogueira**

R. F. Moral, Dr. J. C. Germino, L. G. Bonato, Prof. T. D. Z. Atvars, Prof. R. A. Nome, Prof. A. F. Nogueira
Institute of Chemistry
State University of Campinas (UNICAMP)
Cidade Universitária Zeferino Vaz, Campinas, Sao Paulo – 13083-970, Brazil
E-mail: anafla@unicamp.br, raphael.fmoral@gmail.com

Dr. D. B. Almeida
Instituto de Física Gleb Wataghin
Universidade Estadual de Campinas (UNICAMP)
Cidade Universitária Zeferino Vaz, Campinas, São Paulo – 13083-970, Brasil

Prof. E. M. Therézio
Intitute of Physics
Federal University of Mato Grosso (UFMT)
Quarenta e Nove, 2367, Cuiabá, Mato Grosso – 78060-900, Brazil

Prof. S. D. Stranks
Cavendish Laboratory
JJ Thomson Avenue, Cambridge CB3 0HE, UK
Department of Chemical Engineering and Biotechnology
Philippa Fawcett Drive, Cambridge, CB3 0AS, United Kingdom

Keywords: Two-dimensional metal halides, exciton dynamics, exciton-phonon coupling, soft modes, and phase transition

Abstract: Two-dimensional metal halides semiconductors have been intensively studied in the past few years due to their unique optical properties and potential for new-generation photonic devices. Despite the large number of recent works, this class of materials is still in need of further understanding due to their complex structural and optical characteristics. In this work, a molecular-level explanation for the dual band emission in the two-dimensional $(C_4H_9NH_3)_2PbI_4$ in its bulk form is presented, demonstrating that this feature is caused by a strong exciton-phonon coupling. Temperature-dependent photoluminescence with Raman and infrared spectroscopies reveal that vibrations involving the C-NH_3^+ butylammonium polar head are responsible for this exciton-phonon coupling. Additionally, experimental shifts in the mean phonon frequencies coupled with the electronic excitation, combined with a theoretical model,

show that these vibrational modes present a soft-mode behavior in the phase transition of this material.

1. Introduction

Two-dimensional (2D) metal halides are materials that have been receiving increasing attention in the past few years.[1–4] Owned for their unique optoelectronic properties, these semiconductors are prominent in the development of a series of new-generation photonic devices such as solar cells,[5–8] LEDs,[9–11] and photodetectors.[12–14] Their structure is commonly compared to 3D metal halide perovskites with structure ABX_3 (where A is monovalent cation, B is a divalent cation, more frequently Pb^{2+} and Sn^{2+}, and X is a halide different from F^-) and, very commonly, are regarded as reduced dimensional perovskites or 2D perovskites.[2] The fundamental structural difference between 3D perovskites and 2D metal halides is that, in the latter, the A-site cation is too large to fit the cavity within the octahedrons, generating a layered structure where the inorganic slabs are separated by a bilayer of organic cations (**Figure 1a**).[15] As such, these materials can be regarded as a natural quantum-well (QW) ensemble.[3,16]

Although, to a certain extent, this class of materials do behave like a QW superstructure, presenting excitonic resonance upon optical excitation, their excitonic recombination dynamics are far from trivial. These deviations arise, basically, for two reasons: the dielectric confinement of the exciton due to the organic layers and the influence of these layers in their charge carriers' relaxation/recombination; and the large binding energy of the excitons in these materials.[1,2,17] Thus, 2D metal halides present a complex set of photophysical phenomena such as exciton-phonon coupling,[18,19] polaronic effects,[20–22] self-trapped excitons (STEs)[2,23,24], broad band emission,[25–27] and dark excitonic states.[28,29]

In this work we focus on an intriguing optical feature of the well-known $(BA)_2PbI_4$ (BAPI; BA = butylammonium). This material, in its bulk, microcrystalline form, presents a peculiar dual

band emission that has been receiving increasing attention and is not yet fully understood. An earlier report of this dual band emission was made by Mitzi in 1996.[30] More recently, our group reported similar dual emission profile in this material, and we hypothesized that a strong exciton-phonon coupling could be the reason for the low-energy emission.[31] Also very recently, three distinct works presented different explanations for this dual band, red-shifted emission.[32–34] In the work of Gan *et al.*,[33] the authors show evidences that a thickness-dependent photon recycling effect causes a large red shift in the emission of BAPI micro crystals. However, it is not clear in their work what specifically causes the lower energy emission upon photon recycling. More conclusively, the work of Du *et al*.[32] shows that this dual band is an effect of the stacking slabs in the bulk material: the lower mobility of the organic cations in the bulk (interior of the crystal) causes a residual strain in the lattice; hence, the emission from the bulk is different from the emission from the surface, corroborating previous results,[35] and the dual band profile is a result of this difference. Interestingly, the authors argue that this stacking effect induces a strong exciton-phonon coupling in the bulk material that can be modulated by decreasing the magnitude of the lattice strain. Finally, DeCrescent *et al*.[34] propose that this lower-energy band is a magnetic dipole emission caused by a p-like exciton. This p-like exciton is stabilized at energies below the primary, electric-dipole-emitting 1s exciton *via* self-trapping mechanism. This topic, therefore, is still under intense debate.

Here, we offer a molecular level explanation for this dual band emission of BAPI and draw a general picture underlining this optical property of 2D metal halides. Our temperature-dependent and steady-state optical measurements, combined with Raman and IR spectroscopies, reveal that this low-energy emission is indeed due to a strong exciton-phonon coupling with specific vibration modes that arise from the organic layers. Therefore, a phonon replica of the excitonic state is achieved *via* phonon emission, giving rise to this lower-energy band. In addition, we show that these vibrational modes are also involved in the well-known phase transition in this material, evidenced by the good correlation between temperature-dependent

photoluminescence (PL), X-ray diffraction (XRD) and a soft-mode formalism for phonon-related phase transitions in solids, including perovskites.

2. Structural Characterization

To synthesize the material, we followed a protocol reported by our group.[31] Briefly, in a capped flask, lead iodide is dissolved in a mixture of toluene, butyric acid, and butylamine. In a different flask, butylammonium iodide is dissolved in a similar mixture. The two solutions are swiftly mixed to give an insoluble yellow powder with a noticeable green emission (**Figure 1b**). The suspension is then centrifuged, the yellow powder is separated and washed with clean toluene, and the new suspension is centrifuged again to isolate the clean material. The XRD of the powder is showed in **Figure 1c** along with a reference calculated from single crystal data,[36] and the excellent correlation between the experimental and calculated diffractograms reveals a phase pure material, as previously reported.[31]

To perform the optical measurements in the bulk material, the powder was spread on a glass substrate as shown in the scheme of **Figure 1d**. The wet powder in toluene is placed in one border of the glass substrate, spread over it with the help of a Pasteur pipette, and then is allowed to dry. To prepare thin films, a solution of 80 $mg.mL^{-1}$ of the powder in anhydrous acetonitrile is spin-coated at 3000 rpm for 30 s, as shown in the bottom part of the scheme in **Figure 1d**. The XRD of the thin film is depicted in **Figure S1** in the Supporting Information. It is noteworthy that, in the thin film, a preferential orientation effect in the [00l] direction is observed in the diffractogram. Also, our powder XRD shows a clear asymmetry in diffraction (Lorentzian tail in lower angles), more evident in the peak with index (002), which can be an indication of different lattice parameters between the surface and bulk.[32]

3. Photophysics

In **Figure 2a**, the room-temperature PL spectrum from BAPI shows a broad emission (BE, for simplicity) at lower energy (λ_{max} = 540 nm) alongside a peak we ascribe to the free-exciton (FE) emission (λ_{max} = 520 nm). **Figure 2b** shows the reconstruction of the PL by time-resolved emission spectrum (TRES - inset) measurements in several different times, evidencing a similar profile to the steady state PL (black dotted curve). In addition, the normalized decay curves in **Figure 2c** (taken from horizontal slices of the TRES) show the same decay dynamics in all the emission wavelengths, suggesting that this dual band is not caused by defect states, which would present different decay rates and dynamics. Moreover, in **Figure 2a** – dark blue – the photoluminescence excitation (PLE) spectrum shows that this lower energy band comes from the primary excitonic state, suggesting a dependence of the BE on the FE state.

To understand in depth these emission signatures, we collected temperature-dependent PL spectra (**Figure S2**) and used a theoretical model to discriminate the contributions from acoustic phonons, optical phonons, inhomogeneous broadening, and ionized defects.[37] This model was developed for MQW systems grown by physical methods (*e.g.*, molecular beam epitaxy), but it has been used for 2D metal halides, providing valuable information.[24,25,38] The equation is as follows:

$$\boldsymbol{\Gamma(T) = \Gamma_0 + \Gamma_{ac} T + \Gamma_{opt}(e^{E_{opt}/k_B T} - 1)^{-1} + \Gamma_{in} e^{-E_{in}/k_B T}}$$

where Γ_0 is the temperature-independent linewidth of the emission related to the inhomogeneous broadening; Γ_{ac}, Γ_{opt} are the exciton-phonon coupling parameters for acoustic and optical phonons, respectively; E_{opt} is the energy of the optical phonon that interacts with the exciton; Γ_{in} is the broadening parameter related to ionized defects; and E_{in} is the average binding energy of these defect-emissive states. Hence, by analyzing the dependence of the full width at half maximum (FWHM) of the emission in eV with the temperature, we verify which effects are influencing in the emission dynamics.

For this material, we could not carry out the analysis at lower temperatures due to a phase transition that takes place below 244 K, changing the PL considerably (**Figure 3a**) and causing a discontinuity on the dependence of the FWHM with the temperature. The PL curves were fitted using Voigt functions (a convolution of a Gaussian and a Lorentzian functions) and all the spectra were fitted using two Voigtians (**Figure S3**). Voigt functions yield better fits for peaks that present asymmetric tails such as the red curve in **Figure 2a** (Gaussian in the leftmost side and Lorentzian in the rightmost side). The dependence of the summed FWHM of the two bands with the temperature is shown in **Figure 2d** (blue circles).

For the fit in **Figure 2d** (red line), we set the parameters of the ionized defects to be zero and disregarded the acoustic parameter, considering only the optical phonon contribution and Γ_0

(equation in **Figure 2d**), as reported in other works.[18,21,38] This decision is mathematically and physically justifiable. In mathematical means, the fit with the full equation gives physically unrealistic values of the parameters and large errors (**Figure S4**). However, even with unrealistic parameters, the phonon contribution remained significant, with a phonon energy that is quite consistent: 55 meV, falling in between the two Raman and IR modes in 52 and 59 meV (**Figure 2e**). In physical terms, a few conditions must be considered: 1) The PLE and TRES spectra indicate that these two bands have the same excitonic origin, which suggests that defects do not influence in the emission, in accordance with other reports;[33,35,38] 2) the exciton binding energy and oscillator strength of these materials are high, which explain their predominantly excitonic optical behavior;[30,39] 3) the determined parameters cancelling the ionized-defect term are physically realistic, with acceptable errors; 4) these materials are known to present strong exciton-phonon coupling due to the "softness" of their crystal structure;[16] and 5) the contribution of acoustic phonons is dominant in temperatures below 200 K;[18,37] thus, in the conditions of our analysis, optical phonons are the main homogeneous broadening factor (*i.e.*, Fröhlich scattering).

Considering the above, we fitted the data with the equation shown in the inset of **Figure 2d**, disregarding the effects of ionized defects and acoustic phonons. The resulting fit parameters are shown in **Table 1**. To verify how well the model describes the data, we calculated the $\Gamma(300)$ of the two bands using the parameters determined from the fit and found a total of 226 meV, which is in great accordance with the sum of the FWHM of the two bands from **Figure S3** (230 meV). The large errors associated with each parameter and $\Gamma(300)$ is mainly due to the lack of data points below 242 K, increasing their uncertainty, especially on Γ_0.

The extracted parameters from the model are quite compelling. Γ_0 matches the width of the FE emission, which is expected, since it does not change appreciably with the temperature (**Figure S2**). In MQW systems such as GaAs/AlGaAs, Γ_0 is much lower and the inhomogeneous broadening is attributed, mainly, to deviation in the QW thickness.[37] In 2D metal halides, such as BAPI, the QW thickness is constant (a single layer of $[PbI_6]^{4-}$ octahedrons) and, therefore, does not influence on the inhomogeneous broadening of the emission band. In these systems, therefore, the conformational disorder of the alkyl chains in the bilayer of organic cations is more likely to contribute to the inhomogeneous broadening of their emission linewidths. In addition, the value of the optical-phonon-related term (171 meV – see Supporting Information for details) matches the FWHM of the BE emission, further supporting an exciton-phonon coupling. Interestingly, our work agrees with a recent work from Esmaielpour *et al.* that reported the same 57 meV for the phonon coupled with the low-temperature-phase exciton in

BAPI (FE_{242}; see **Figure 3a**).[38] Given the unusual high energy of this phonon, the authors suggested that it is due to a strong polaronic effect in the system.

Here, we propose a different picture. This high-energy phonon matches, within the errors, the vibrational modes observed in Raman and IR (52 and 59 meV – **Figure 2e**), and these modes are due to the organic layers of butylammonium cations. Strikingly, these modes are associated with the C-N and -NH_3 bonds vibrations of the polar heads of butylammonium cations bound to the inorganic structure.[40,41] Therefore, this high-energy phonon is due to these vibrational modes that are not isolated from the inorganic cage motions and, therefore, can couple with the exciton. This direct correlation, to the best of our knowledge, has not been considered before. In the work of Esmaielpour *et al*., the authors report many phonon replicas of the FE emission at 4.2 K. Notably, a replica that is 39 meV away from the FE peak, that the authors label as P7, is consistent to the 57 meV we found in our analysis at temperatures above 242 K, further supporting our conclusion. Moreover, Li *et al*.[42] also reported a similar phonon replica, and correlated it to a Raman frequency, at 78 K, of 237 cm^{-1}. Although the authors did not assign this frequency to any specific vibration, it is in the range of the torsional oscillation about the C-N bond in BA.[40] **Table 2** shows the origin of these vibrational modes and their common frequencies.

In **Table 2**, we observe that the frequencies presented are the peaks in the Raman spectrum from 371 to 476 cm^{-1} in **Figure 2e**. All these modes are related to the C-NH_3^+ vibrations in the solid state. Note that, even the otherwise inactive modes, can be active upon coupling with the inorganic structure motions, as discussed in the work of Leguy *et al*.[43] As thus, our results strongly indicates that the modes in **Table 2** (*e.g.*, mode #4) are responsible for the strong exciton-phonon we observe in this work.

In addition, our findings are experimental evidences for the predictions from the work of Zhang *et al*.[44] In their report they used molecular nonadiabatic simulations combined with density functional theory calculations to evaluate the impact of the organic molecules in 2D $BA_2[MAPbI_3]PbI_4$ and 3D $MAPbI_3$ (MA = methylammonium) on the charge carrier dynamics. They found that coupled vibrational modes between the BA^+ cations and the Pb-I framework are responsible for the fast hot-carriers relaxation *via* strong electron-phonon coupling. Hence, our results are fully consistent with their predictions. In our case, however, these coupled vibrational modes influence not only the hot-carrier relaxation, but also the excitonic recombination. These findings explain both the origin of the unusual dual band and the high-energy phonon extracted from the temperature-dependent PL. The strong exciton-phonon coupling is evidenced by the high Γ_{opt} value in **Table 1**.

The PL spectrum of BAPI thin films (**Figure S5**) presents only the FE emission. This suggests that this dual band is most likely a property of the bulk material, as previously reported.[32,35] In addition, our time-correlated single-photon counting (TCSPC) measurements show that the recombination rates in the thin film samples are faster than the rates determined from the powder sample (**Figure S6 – S11** and **Tale S1**). This divergence comes from the fact that this strong exciton-phonon is mainly, if not solely, observed in the bulk and that effects such as photon recycling, which would further increase the recombination rate, are thickness dependent.[33] Furthermore, we also verified that the decay curves of the powder BAPI (**Figure S9 – S14**) show a multiexponential profile, reflecting these different decay channels upon photoexcitation.

Another evidence for the distinct behavior between bulk and surface is the difference in the phase transition temperature in these systems (**Figure S15** shows a scheme of this phase transition). The phase transition in the thin film is well above of that for the powder. To verify this difference, we analyzed the ratio of the integrated areas of the PL peaks during the phase transition, for both the thin film and powder. **Figure 3a** shows the temperature-dependent PL of the powder BAPI below 242 K, where the phase transition starts, and **Figure 3b** shows the temperature-dependent powder XRD of the material on the peak with Miller index (002) (the complete diffractograms are depicted in **Figure S16**). Both PL and XRD data show that the transition takes place between 242 K and 230 K, approximately, as can be seen in **Figure 3c**. On the contrary, the thin film transition temperature, extracted from temperature-dependent PL, is at about 270 K, taking place between 278 and 260 K (**Figure S17**). This drastic difference further reflects the bulk effect in the optical and structural properties of this material and offers further support to our assignments regarding the dual emission.

4. Phase Transition and Soft Modes

At last, we reveal an interesting property of BAPI regarding the vibrational coupling in the exciton recombination dynamics and the phase transition. As proposed in a previous report,[45] these modes involving the C-NH_3^+ bonds may present a soft-mode behavior. Soft modes are normal vibration modes of the crystal lattice that suffer changes in their fundamental frequency as the phase transition approaches. As such, the coupling between these soft modes and other degrees of freedom in a given solid (*e.g.*, electronic, vibrational, magnetic, etc.) provide ways to probing physical properties that are indirectly affected by the phase transition.[46] Given the consistency of the PL data with the XRD in assessing the phase transition, we hypothesized that the vibrational modes found through the PL analysis could indeed present a soft-mode behavior.

To verify our conjecture, we used a formalism based on changes in the mean frequency of these lattice vibrations during the phase transition in solids.[47,48]

Figure 3a shows that the PL intensity decreases as the temperature increases from 208 K to 242 K, and the PL line shapes show an interconversion between two excitonic states. In order to compare the experimental results with this microscopic model of structural phase transitions in solids, the PL data, in the range from 302 to 232 K, were used to calculate the variation of the phonon frequencies coupled to the electronic excitation with the temperature (see **Figure S2a**). The black circles in **Figure 3d** are experimental variations in the phonon frequencies. The two solid curves are calculated from the real (harmonic) part of the equation below:[48]

$$\boldsymbol{\omega(T) = \omega_0 (T_0 - T)^{1/3}}$$

with ω_0 = 419 cm^{-1} (52 eV) and 476 cm^{-1} (59 eV), taken from the Raman frequencies in **Figure 2e**, T_0 = 230 K (*i.e.*, the end of the phase transition) and the 1/3 exponent denotes a second-order phase transition with short-range correlations near the transition point, consistent with smooth extrapolation of $\omega(T)$ to zero as $T \rightarrow T_0$.[48] Note that the expression has no adjustable parameters. The good agreement between experiment and theory, combined with the XRD data, provides a microscopic picture of the phase transition and the description of the nature of the order parameter in terms of specific phonon frequencies and atomic displacements.

This last consideration encloses the picture reported in this work: vibrational modes from the organic moieties, intimately bonded to the inorganic framework, couple with excitons, originating an excitonic replica in lower energies. The broad nature of the two bands are related to the inhomogeneities (*e.g.*, imperfections in the alignment of the alkyl chains in the bilayer of BA cations) in the bulk material; this statistical disorder influence in both electronic and vibrational degrees of freedom, resulting in the large FWHM (230 meV) observed in the dual band emission of BAPI. Therefore, this dual band seems to result from an interplay between the lattice dynamical disorder in the interior of the crystal and the strong exciton-phonon coupling with vibrations from BA^+ polar heads. Additionally, our analysis show that these vibrational modes behave like soft modes in the phase transition of BAPI. This assignment is consistent, given the well-known dependence of the inorganic structure of 2D metal halides with the organic cation[36,49] and considering the fact that these modes are related to the vibrating C-NH_3^+ polar head of butylammonium associated with the inorganic cage. To summarize the picture drawn in this work, we present a scheme in **Figure 4**.

5. Conclusions

In this work we investigated in depth a hotly debated optical feature of a well-known 2D lead halide, $(BA)_2PbI_4$. We found that specific vibrational modes related to the C-NH_3^+ moiety in BA cations couples with the exciton, splitting the excitonic emission into two bands. The energy of these vibrational modes and their influence in the charge carriers' dynamics are in accordance with recent reports. In addition, comparing our experimental data with a theoretical model, we demonstrated that these vibrational modes present a soft-mode behavior in the phase transition of the material. This work offers a new perspective for the understanding of the optical and structural properties of 2D metal halide systems that are under intense discussion in the last years. Advancing in the fundamentals of these systems is of primordial importance to apply these materials to a new generation of optoelectronic devices.

6. Experimental Section

Materials: lead iodide (99%), hydroiodic acid (57% in H_2O), butylamine (99.5%), butyric acid (≥99%), and anhydrous toluene were all purchased from Sigma Aldrich and used as received. Butylammonium iodide was synthesized by reacting butylamine with HI in water. The white solid was obtained by removing the water under reduced pressure, and it was dried in a desiccator with P_2O_5 under reduced pressure.

Synthesis of $(BA)_2PbI_4$ (BAPI): in a capped flask, lead iodide (96 mg, 0.2 mmol) is dissolved in toluene (5 mL), butyric acid (1 mL), and butylamine (0.4 mL). In a different flask, butylammonium iodide (80.4 mg, 0.42 mmol) is dissolved in toluene (3 mL), butyric acid (1 mL), and butylamine (0.1 mL). The two solutions are swiftly mixed to give an insoluble yellow powder. This powder is separated by centrifugation at 3000 rpm, washed with clean toluene, and separated by centrifugation again. The material is bright yellow and presents a clear green emission even in the solid form. To prepare a film of this powder, the wet pellet in toluene is simply spread over a glass substrate with the help of a Pasteur pipette, and then allowed to dry. The thin films are prepared by spin-coating a solution ca. 80 $mg.mL^{-1}$ and at 3000 rpm for 30 s in a clean glass substrate (pre-treatment of the substrates with UV/ozone results in smoother films).

Absorption Spectrum on the Solid: spectra were measured in a Shimadzu UV 2450 equipment. A smooth pallet of powder Ba_2SO_4 was used as the reference for 100% reflectance.

Absorption Spectra on the Thin Films: absorbance in thin films was measured in an Agilent Carry 60 UV-vis equipment in transmission mode. A glass substrate was used for the base line subtraction.

Temperature-Dependent and Steady-State Photoluminescence and Photoluminescence Excitation Spectra: spectra were collected in a Horiba-JOBINYVON Fluorolog-3. The excitation source was perpendicular to the film, and the emission was collected at an angle of approximately 15°. A 450 nm optical filter was used to eliminate scattering artefacts. Data were corrected according to the lamp and detector fluctuations (xenon lamp) with correction algorithms from the equipment software. The temperature series were measured with the help of a Linkam THMS600 (Linkam Scientific Instruments) attachment for temperature and environmental control. Two optical fibers were directed to the Linkam window with similar geometry for excitation and emission collection. The sample was allowed to thermalize for five minutes from one measurement to another.

Time-Correlated Single-Photon Counting and Time-Resolved Photoluminescence Spectra: the decay curves were measured in an Edinburg Analytical Instruments FL 900 spectrofluorometer with an MCP-PMT (Hamamatsu R3809U-50; 50 ps). These measurements were carried out with a laser EPL 375 and excitation wavelength of (375 ± 5) nm and pulse width of 65 ps (at 10 MHz). The software used for the fittings was the FAST software from Edinburg Instruments. The laser fluence in the measurements was 9.6 $mW.cm^{-2}$ per pulse.

Temperature-Dependent Powder X-ray Diffraction: diffractograms were collected in a Rigaku DMAX equipment with a temperature range from 25 to 300 K. Diffractogram were register with a Cu Kα source (1.5406 Å), steps of 0.03 2θ ° and integration time of 5 s. The sample was allowed to thermalize a few minutes from one measurement to another.

Raman Spectrum: the spectrum was collected in custom instrumental setup. The sample was excited with a 785 nm laser (Cobolt 08 series 0785-08-11-0500-200). The laser power on the sample was 20 mW. The instrument was equipped with a series of VBG filters (OptigrateRFS-785-OD4-11 M) to minimize attenuated spontaneous emission and Rayleigh scattering. Several optical components such as lenses, slits, optical fiber, and mirrors were used to guide, collect, and focus the excitation laser and the Raman scattering radiation. A monochromator (Andor/Ox-ford SR-500i-C-SIL) was coupled to a CCD camera (Andor/Oxford iDUS 416 - DU416A-LDC-DD) with which the spectral signal was registered. The spectrum was registered in a frequency range from -1000 to 2000 cm^{-1} with signal accumulation of 60 images with an integration time of 0.5 s each (30 s total). More details of the instrumental setup and characteristics can be found in the work of Paiva *et al*.,[50] who kindly allowed and helped us measure the Raman spectrum in their laboratory.

Temperature Dependent Photoluminescence of the Thin Films: thin films were excited with a diode 405 nm laser (LaserLine-iZi) with a power density <20 $mW.cm^{-2}$. Temperature was controlled using a He closed cycle cryostat with a range from 10 to 290 K, under vacuum. The spectral signal was collected in an Ocean Optics USB2000 spectrometer.

Fourier Transform Infrared Spectroscopy: the spectrum was acquired through a Cary 630 FTIR spectrometer using Attenuated Total Reflectance (ATR) acquisition mode.

Supporting Information

Supporting Information is available from the Wiley Online Library or from the author.

Acknowledgements

RFM acknowledges the support from FAPESP – process number: 2019/25765-6. AFN, JCG and RFM gratefully acknowledge support from FAPESP (the Sao Paulo Research Foundation, Process 2017/11986-5), Shell, and the strategic importance of the support given by ANP (Brazil's National Oil, Natural Gas and Biofuels Agency) through the R&D levy regulation. SDS acknowledges the Royal Society and Tata Group (UF150033). DBA thanks the support of

CAPES and FAPESP (process 2019/22576-8). TDZA acknowledges the support from FAPESP – process number: 2013/16245-2. We also thank Professor Alexandre Marletta, from Federal University of Uberlândia, for kindly allowing us to measure temperature-dependent PL of the thin films in his laboratory.

Received: ((will be filled in by the editorial staff))
Revised: ((will be filled in by the editorial staff))
Published online: ((will be filled in by the editorial staff))

References

[1] K. Leng, W. Fu, Y. Liu, M. Chhowalla, K. P. Loh, *Nat. Rev. Mater.* **2020**, *5*, 482.

[2] M. D. Smith, B. A. Connor, H. I. Karunadasa, *Chem. Rev.* **2019**, *119*, 3104.

[3] C. M. Mauck, W. A. Tisdale, *Trends Chem.* **2019**, *1*, 380.

[4] F. Zhang, H. Lu, J. Tong, J. J. Berry, M. C. Beard, K. Zhu, *Energy Environ. Sci.* **2020**, *13*, 1154.

[5] D. Lu, G. Lv, Z. Xu, Y. Dong, X. Ji, Y. Liu, *J. Am. Chem. Soc.* **2020**, *142*, 11114.

[6] Y. Dong, D. Lu, Z. Xu, H. Lai, Y. Liu, *Adv. Energy Mater.* **2020**, 2000694.

[7] P. Cheng, Z. Xu, J. Li, Y. Liu, Y. Fan, L. Yu, D.-M. Smilgies, C. Müller, K. Zhao, S. F. Liu, *ACS Energy Lett.* **2018**, *3*, 1975.

[8] H. Ren, S. Yu, L. Chao, Y. Xia, Y. Sun, S. Zuo, F. Li, T. Niu, Y. Yang, H. Ju, B. Li, H. Du, X. Gao, J. Zhang, J. Wang, L. Zhang, Y. Chen, W. Huang, *Nat. Photonics* **2020**, *14*, 154.

[9] P. Vashishtha, M. Ng, S. B. Shivarudraiah, J. E. Halpert, *Chem. Mater.* **2019**, *31*, 83.

[10] H. Chen, J. Lin, J. Kang, Q. Kong, D. Lu, J. Kang, M. Lai, L. N. Quan, Z. Lin, J. Jin, L. Wang, M. F. Toney, P. Yang, *Sci. Adv.* **2020**, *6*, eaay4045.

[11] H. Tsai, W. Nie, J.-C. Blancon, C. C. Stoumpos, C. M. M. Soe, J. Yoo, J. Crochet, S. Tretiak, J. Even, A. Sadhanala, G. Azzellino, R. Brenes, P. M. Ajayan, V. Bulović, S. D. Stranks, R. H. Friend, M. G. Kanatzidis, A. D. Mohite, *Adv. Mater.* **2018**, *30*,

1704217.

[12] J. Wang, J. Li, S. Lan, C. Fang, H. Shen, Q. Xiong, D. Li, *ACS Nano* **2019**, *13*, 5473.

[13] Y. Zhao, Y. Qiu, H. Gao, J. Feng, G. Chen, L. Jiang, Y. Wu, *Adv. Mater.* **2020**, *32*, 1905298.

[14] J. Li, J. Wang, J. Ma, H. Shen, L. Li, X. Duan, D. Li, *Nat. Commun.* **2019**, *10*, 806.

[15] C. C. Stoumpos, D. H. Cao, D. J. Clark, J. Young, J. M. Rondinelli, J. I. Jang, J. T. Hupp, M. G. Kanatzidis, *Chem. Mater.* **2016**, *28*, 2852.

[16] D. B. Straus, C. R. Kagan, *J. Phys. Chem. Lett.* **2018**, *9*, 1434.

[17] C. Katan, N. Mercier, J. Even, *Chem. Rev.* **2019**, *119*, 3140.

[18] L. Ni, U. Huynh, A. Cheminal, T. H. Thomas, R. Shivanna, T. F. Hinrichsen, S. Ahmad, A. Sadhanala, A. Rao, *ACS Nano* **2017**, *11*, 10834.

[19] D. B. Straus, S. Hurtado Parra, N. Iotov, J. Gebhardt, A. M. Rappe, J. E. Subotnik, J. M. Kikkawa, C. R. Kagan, *J. Am. Chem. Soc.* **2016**, *138*, 13798.

[20] F. Thouin, D. A. Valverde-Chávez, C. Quarti, D. Cortecchia, I. Bargigia, D. Beljonne, A. Petrozza, C. Silva, A. R. Srimath Kandada, *Nat. Mater.* **2019**, *18*, 349.

[21] S. Neutzner, F. Thouin, D. Cortecchia, A. Petrozza, C. Silva, A. R. Srimath Kandada, *Phys. Rev. Mater.* **2018**, *2*, 064605.

[22] D. Cortecchia, J. Yin, A. Bruno, S.-Z. A. Lo, G. G. Gurzadyan, S. Mhaisalkar, J.-L. Brédas, C. Soci, *J. Mater. Chem. C* **2017**, *5*, 2771.

[23] T. Hu, M. D. Smith, E. R. Dohner, M.-J. Sher, X. Wu, M. T. Trinh, A. Fisher, J. Corbett, X.-Y. Zhu, H. I. Karunadasa, A. M. Lindenberg, *J. Phys. Chem. Lett.* **2016**, *7*, 2258.

[24] E. R. Dohner, A. Jaffe, L. R. Bradshaw, H. I. Karunadasa, *J. Am. Chem. Soc.* **2014**, *136*, 13154.

[25] K. Thirumal, W. K. Chong, W. Xie, R. Ganguly, S. K. Muduli, M. Sherburne, M. Asta, S. Mhaisalkar, T. C. Sum, H. Sen Soo, N. Mathews, *Chem. Mater.* **2017**, *29*, 3947.

[26] A. Yangui, D. Garrot, J. S. Lauret, A. Lusson, G. Bouchez, E. Deleporte, S. Pillet, E. E. Bendeif, M. Castro, S. Triki, Y. Abid, K. Boukheddaden, *J. Phys. Chem. C* **2015**, *119*, 23638.

[27] M. D. Smith, H. I. Karunadasa, *Acc. Chem. Res.* **2018**, *51*, 619.

[28] G. Folpini, D. Cortecchia, A. Petrozza, A. R. Srimath Kandada, *J. Mater. Chem. C* **2020**, *8*, 10889.

[29] H. Fang, J. Yang, S. Adjokatse, E. Tekelenburg, M. E. Kamminga, H. Duim, J. Ye, G. R. Blake, J. Even, M. A. Loi, *Adv. Funct. Mater.* **2020**, *30*, 1907979.

[30] D. B. Mitzi, *Chem. Mater.* **1996**, *8*, 791.

[31] R. F. Moral, L. G. Bonato, J. C. Germino, W. X. Coelho Oliveira, R. Kamat, J. Xu, C. J. Tassone, S. D. Stranks, M. F. Toney, A. F. Nogueira, *Chem. Mater.* **2019**, *31*, 9472.

[32] Q. Du, C. Zhu, Z. Yin, G. Na, C. Cheng, Y. Han, N. Liu, X. Niu, H. Zhou, H. Chen, L. Zhang, S. Jin, Q. Chen, *ACS Nano* **2020**, *14*, 5806.

[33] Z. Gan, X. Wen, W. Chen, C. Zhou, S. Yang, G. Cao, K. P. Ghiggino, H. Zhang, B. Jia, *Adv. Energy Mater.* **2019**, *9*, 1900185.

[34] R. A. DeCrescent, X. Du, R. M. Kennard, N. R. Venkatesan, C. J. Dahlman, M. L. Chabinyc, J. A. Schuller, *ACS Nano* **2020**, *14*, 8958.

[35] T. Sheikh, A. Shinde, S. Mahamuni, A. Nag, *ACS Energy Lett.* **2018**, *3*, 2940.

[36] D. G. Billing, A. Lemmerer, *Acta Crystallogr. Sect. B Struct. Sci.* **2007**, *63*, 735.

[37] J. Lee, E. S. Koteles, M. O. Vassell, *Phys. Rev. B* **1986**, *33*, 5512.

[38] H. Esmaielpour, V. R. Whiteside, S. Sourabh, G. E. Eperon, J. T. Precht, M. C. Beard, H. Lu, B. K. Durant, I. R. Sellers, *J. Phys. Chem. C* **2020**, *124*, 9496.

[39] T. Ishihara, J. Takahashi, T. Goto, *Solid State Commun.* **1989**, *69*, 933.

[40] George Socrates, *Infrared and Raman Characteristic Group Frequencies: Tables and Charts*, John Wiley & Sons, **2004**.

[41] H. Abid, A. Trigui, A. Mlayah, E. K. Hlil, Y. Abid, *Results Phys.* **2012**, *2*, 71.

[42] W. Li, C. Fang, H. Wang, S. Wang, J. Li, J. Ma, J. Wang, H. Luo, D. Li, *Nano Res.* **2019**, *12*, 2858.

[43] A. M. A. Leguy, A. R. Goñi, J. M. Frost, J. Skelton, F. Brivio, X. Rodríguez-Martínez, O. J. Weber, A. Pallipurath, M. I. Alonso, M. Campoy-Quiles, M. T. Weller, J. Nelson, A. Walsh, P. R. F. Barnes, *Phys. Chem. Chem. Phys.* **2016**, *18*, 27051.

[44] S.-F. Zhang, X.-K. Chen, A.-M. Ren, H. Li, J.-L. Bredas, *ACS Energy Lett.* **2019**, *4*, 17.

[45] M. Couzi, A. Daoud, R. Perret, *Phys. Status Solidi* **1977**, *41*, 271.

[46] P. A. Fleury, *Annu. Rev. Mater. Sci.* **1976**, *6*, 157.

[47] J. Feder, E. Pytte, *Phys. Rev. B* **1970**, *1*, 4803.

[48] J. F. Scott, *Rev. Mod. Phys.* **1974**, *46*, 83.

[49] M. E. Kamminga, H.-H. Fang, M. R. Filip, F. Giustino, J. Baas, G. R. Blake, M. A. Loi, T. T. M. Palstra, *Chem. Mater.* **2016**, *28*, 4554.

[50] E. M. Paiva, R. L. Ribessi, C. F. Pereira, J. J. R. Rohwedder, *Spectrochim. Acta Part A Mol. Biomol. Spectrosc.* **2020**, *228*, 117798.

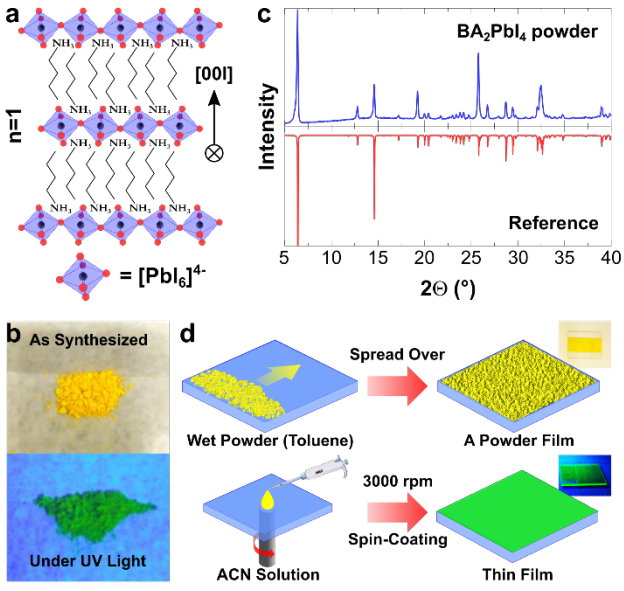

Figure 1. a) Schematic representation of the crystalline structure of BA_2PbI_4; b) the microcrystalline material as synthesized and under UV light; c) powder XRD pattern along with the reference calculated from single crystal data; d) schemes showing the powder and thin film preparations.

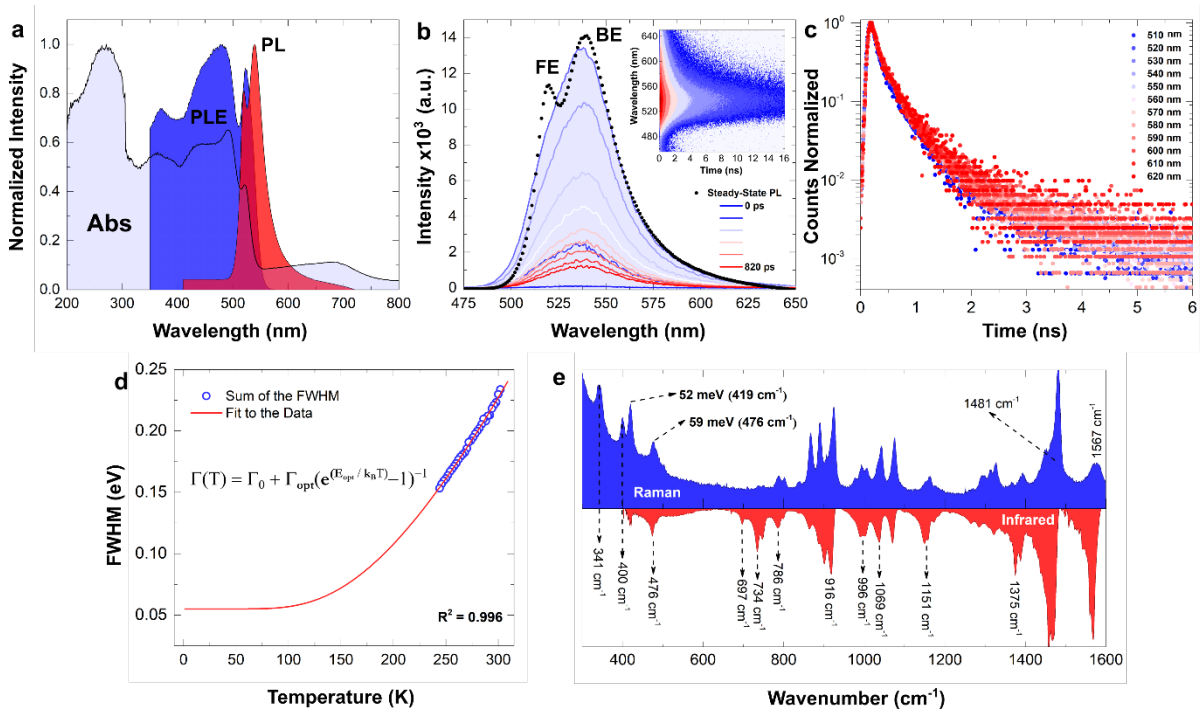

Figure 2. Optical and vibrational spectra of powder BA_2PbI_4: a) absorption (light blue), emission at 375 nm (red), and PLE at 600 nm (dark blue) spectra; b) time-resolved PL spectra reconstruction in different times (the inset is the TRES color map; laser fluence = 9.6 $mW.cm^{-2}$ per pulse); c) normalized time-correlated single-photon counting decays in several wavelengths (taken from the TRES in b); d) FWHM variation with temperature of the two emission bands at 520 nm and 540 nm summed – the inset is the equation used for the fit; e) Raman and attenuated total reflectance infrared spectra.

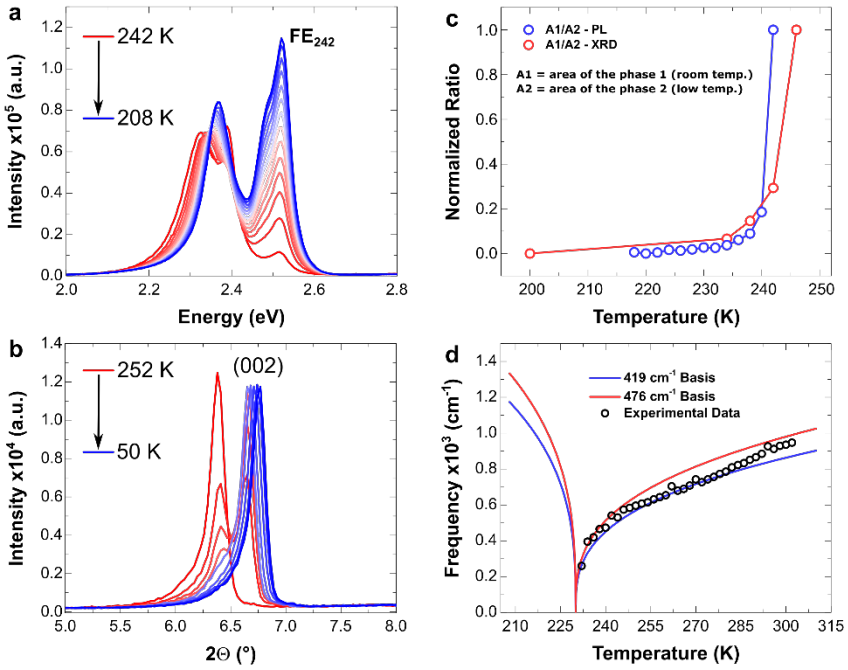

Figure 3. a) temperature-dependent PL of the powder $(BA_2)PbI_4$; b) temperature-dependent XRD of the powder, showing the peak with Miller index (002); c) ratio of the integrated areas of the peaks in the PL and XRD – A1 is the peak of the room-temperature phase and A2 is the peak of the low-temperature phase; d) comparison of the phonon-assisted phase transition model using two fundamental frequencies with our experimental data.

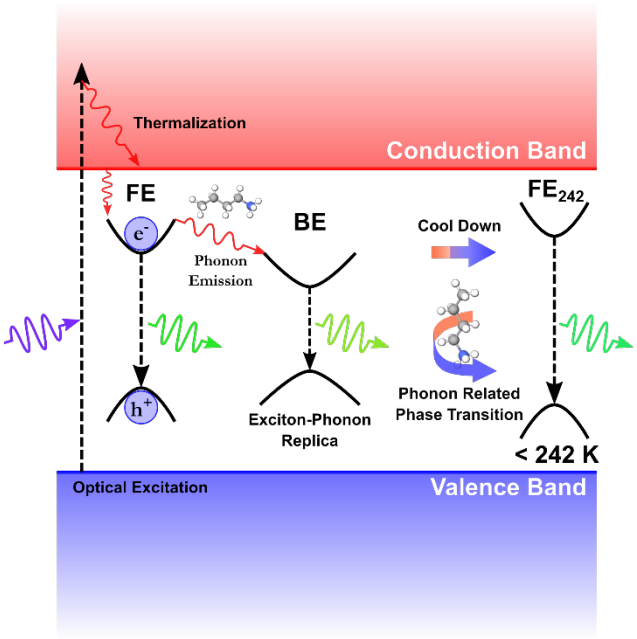

Figure 4. Summary of the structural and optical phenomena reported in this work. Upon optical excitation, hot carriers are generated, relaxing to the excitonic state. From this state, we observe either excitonic or phonon emission, the latter generating an emissive exciton-phonon replica. Lastly, as the temperature decreases, a phonon-related phase transition takes place, and a different excitonic state emerges.

Table 1. Fit parameters extracted from the analysis of the temperature dependence of the FWHM in the PL

Γ_0 [meV]	Γ_{opt} [meV]	E_{opt} [meV]	Γ(300) [meV]
55 ± 25	1396 ± 600	57 ± 14	226 ± 205

Table 2. Vibrational modes related to the C-NH_3^+ moiety of butylammonium cations[40,41]

#	Frequency [cm^{-1}]	Raman	IR	Vibration
1	250 – 370	-	-	CCN twis./NH_3^+ def. vib.
2	310 – 410	w - m	-	CCN wagging vib.
3	315 – 465	w	w - m	C-N def. vib.
4	425 – 535	-	w - m	NH_3^+ twis./CCN def. vib.

[a] **twis.** = twisting; [b] **def.** = deformation; [c] **vib.** = vibration(s); [d] **w** = weak; [e] **m** = medium; [f] **dash** = inactive

This work demonstrates the molecular origin of a dual band emission observed in 2D lead halides. Coupled vibrational modes from the organic/inorganic moieties causes this strong exciton-phonon coupling. Additionally, the correlation between a theoretical formalism with PL and XRD reveals that these vibrational modes present a soft-mode behavior.

[1]Raphael F. Moral, [1]José C. Germino, [1]Luiz G. Bonato, [2]Diogo B. Almeida, [1,3]Eralci M. Therézio, [1]Teresa D. Z. Atvars, [4,5]Samuel D. Stranks, [1]René A. Nome, and [1]Ana F. Nogueira**

Influence of the Vibrational Modes from the Organic Moieties in Two-Dimensional Lead Halides on Excitonic Recombination and Phase Transition

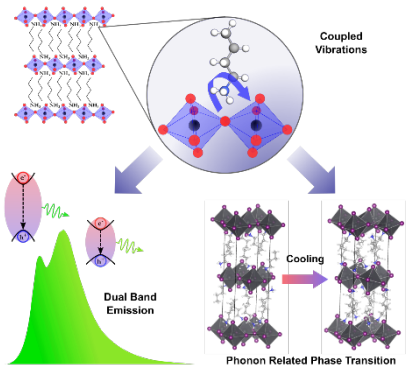

Supporting Information

Influence of the Vibrational Modes from the Organic Moieties in Two-Dimensional Lead Halides on Excitonic Recombination and Phase Transition

[1]Raphael F. Moral, [1]José C. Germino, [1]Luiz G. Bonato, [2]Diogo B. Almeida, [1,3]Eralci M. Therézio, [1]Teresa D. Z. Atvars, [4,5]Samuel D. Stranks, [1]René A. Nome, and [1]Ana F. Nogueira**

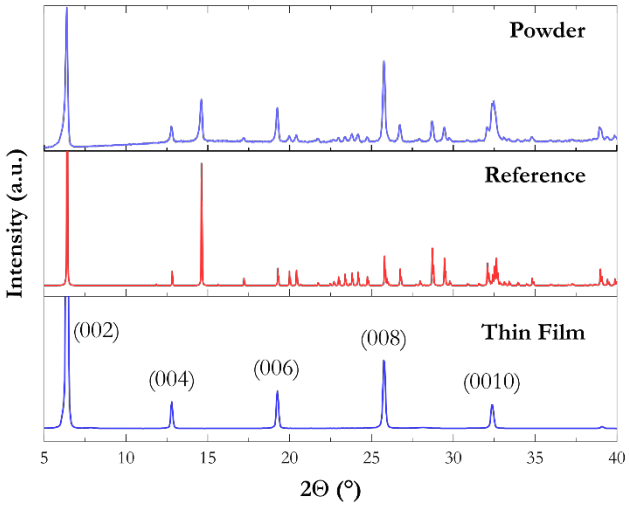

Figure S1. Powder and thin film XRD of $(BA)_2PbI_4$ along with its reference calculated from single crystal data.

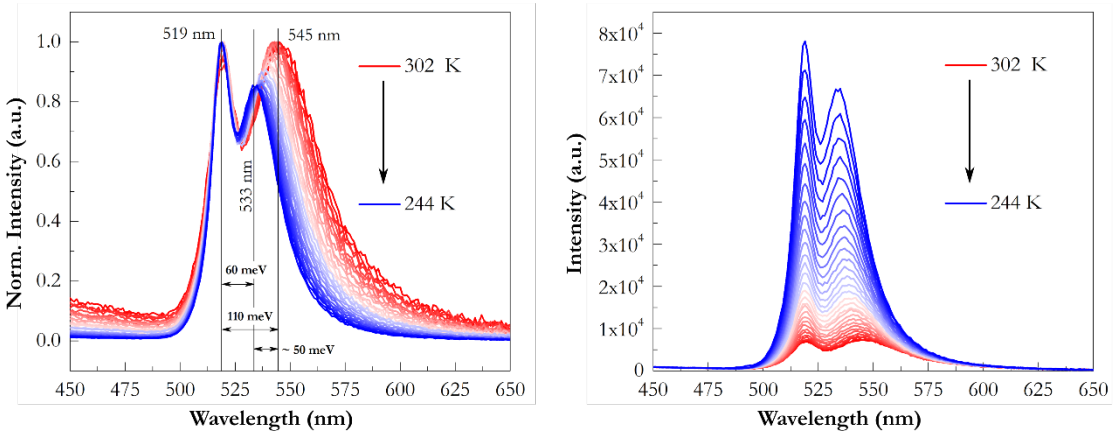

Figure S2. Temperature-dependent PL spectra of powder $(BA)_2PbI_4$ before the phase transition.

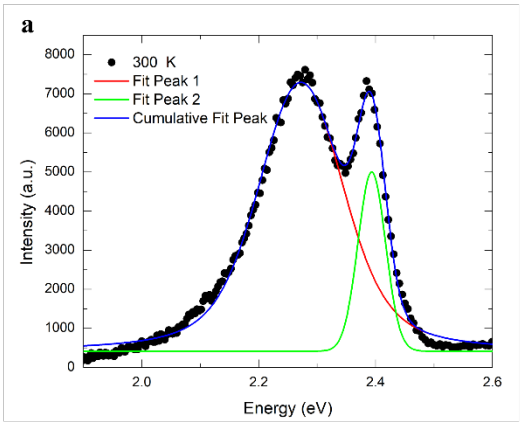

Model	Voigt		
Equation	y = nlf_voigt(x,y0,xc,A,wG,wL) ;		
Reduced Chi-Sqr	85243.90085		
Adj. R-Square	0.98256		
		Value	Standard Error
Peak1(Intensity)	y0	416.95775	36.93212
Peak1(Intensity)	xc	2.27235	0.00133
Peak1(Intensity)	A	1511.71459	51.32306
Peak1(Intensity)	wG	0.13062	0.01003
Peak1(Intensity)	wL	0.07345	0.01211
Peak1(Intensity)	FWHM	0.17429	0.0038
Peak2(Intensity)	y0	416.95775	36.93212
Peak2(Intensity)	xc	2.39347	8.94202E-4
Peak2(Intensity)	A	270.81999	13.86479
Peak2(Intensity)	wG	0.05552	0.00239
Peak2(Intensity)	wL	1.67636E-20	--
Peak2(Intensity)	FWHM	0.05552	0.00239

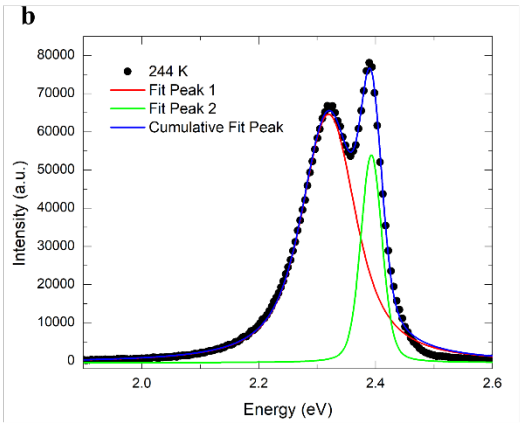

Model	Voigt		
Equation	y = nlf_voigt(x,y0,xc,A,wG,wL);		
Reduced Chi-Sqr	727798.90525		
Adj. R-Square	0.99802		
		Value	Standard Error
Peak1(Intensity)	y0	-438.03451	81.76417
Peak1(Intensity)	xc	2.31968	6.12683E-4
Peak1(Intensity)	A	10163.93965	159.89062
Peak1(Intensity)	wG	0.05781	0.00312
Peak1(Intensity)	wL	0.07868	0.00259
Peak1(Intensity)	FWHM	0.11049	0.00128
Peak2(Intensity)	y0	-438.03451	81.76417
Peak2(Intensity)	xc	2.39285	2.82868E-4
Peak2(Intensity)	A	2716.7716	118.44113
Peak2(Intensity)	wG	0.03714	0.00161
Peak2(Intensity)	wL	0.00995	0.00277
Peak2(Intensity)	FWHM	0.04275	7.56702E-4

Figure S3. Examples of the fits of the two emission bands using Voigtian functions **a)** PL spectrum at 300 K along with a table showing its fit parameters and **b)** PL spectrum at 244 K along with a table showing its fit parameters.

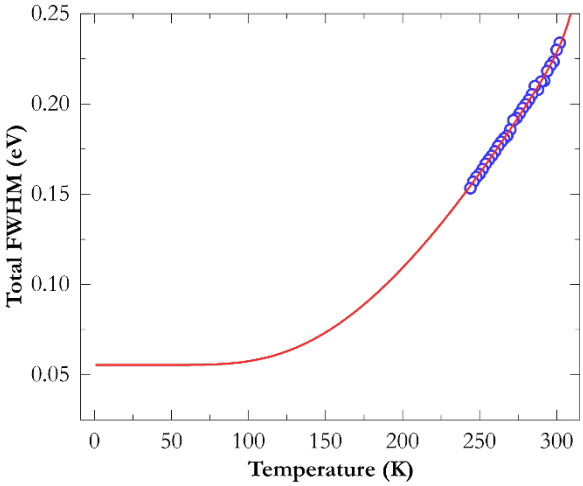

Model	BroadeningModel (User)		
Equation	Go+(Gac*T)+(Gph/((exp(Eph/(Kb*x)))-1))+(Gin*exp(-Ein/(Kb*x)))		
Reduced Chi-Sqr	1.70331E-6		
Adj. R-Squar	0.99683		
		Value	Standard Err
FWHM Total	Go	0.04885	8813.70981
	Gph	1.27074	1.75954
	Gin	2.63357E1	2.08627E20
	Eph	0.05519	0.04013
	Ein	1.24837	2.34489
	Gac	0.00152	2049.22339

Figure S4. Example of the fit of the temperature-dependent PL data using the full equation and its table containing the parameters of the fit. The reddish rectangles emphasize the phonon energies that is close to the 57 meV reported in the main text.

Calculation of *Γ(300)*

By calculating the *Γ(300)* using the parameters determined (shown in **Table 1** of the main text), we find FWHM values of the peaks in close agreement with the experimental data. The calculations are shown below:

$$\Gamma(T) = \Gamma_0 + \Gamma_{opt}(e^{E_{opt}/k_BT} - 1)^{-1}$$

$$\Gamma(300) = 0.055 + 1.3964(e^{0.0571/0.0258} - 1)^{-1}$$

$$\Gamma(300) = 0.055 + 0.1714$$

$$\Gamma(300) = 0.226\ eV\ or\ 226\ meV$$

The result emphasized in blue is in close agreement with the summed FWHM of the two emission bands at 300 K from the table in **Figure S3a** (229.8 meV).

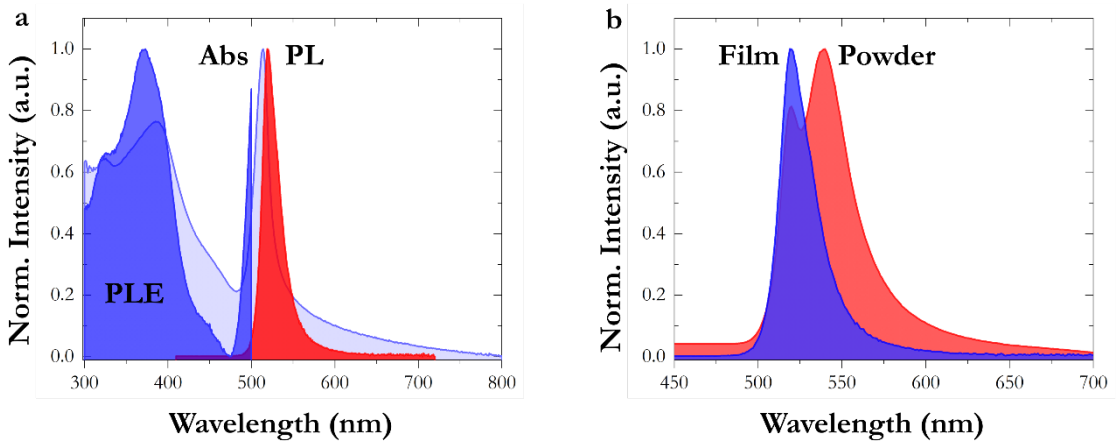

Figure S5. a) absorption (light blue), emission at 375 nm (red), and PLE at 520 nm (dark blue) spectra of the thin film of $(BA)_2PbI_4$ **b)** overlap of the emission from the powder (red) and the emission from the thin film (blue) both at 375 nm excitation.

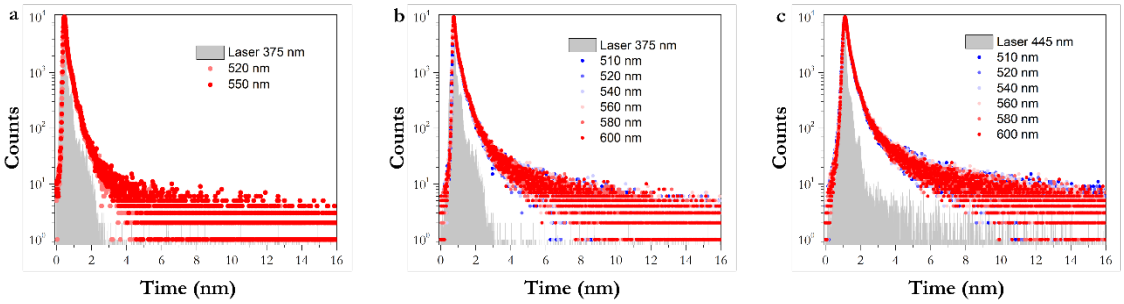

Figure S6. Time-correlated single-photon counting (TCSPC) of $(BA)_2PbI_4$ using a 375 nm and 445 nm lasers (Fluence = 9.6 $mW.cm^{-2}$ per pulse) **a)** thin film; **b)** powder with 375 nm; and **c)** powder with 445 nm. A tri-exponential function offered the best fit for the decays.

From **Figure S6**, it is clear the difference in the TCSPC dynamics in the thin film. The decay curves of the powder have a visible slower rate with a component with a longer delay time (~1 ns), as can be verified in **Figure S9 – S14**. For the powder, within the same excitation energy, the decay dynamics are the same. However, comparing the two excitation wavelengths (375 nm and 445 nm), the contribution of each decay channel changes (evidenced by different B_i values) and the rates are slightly different.

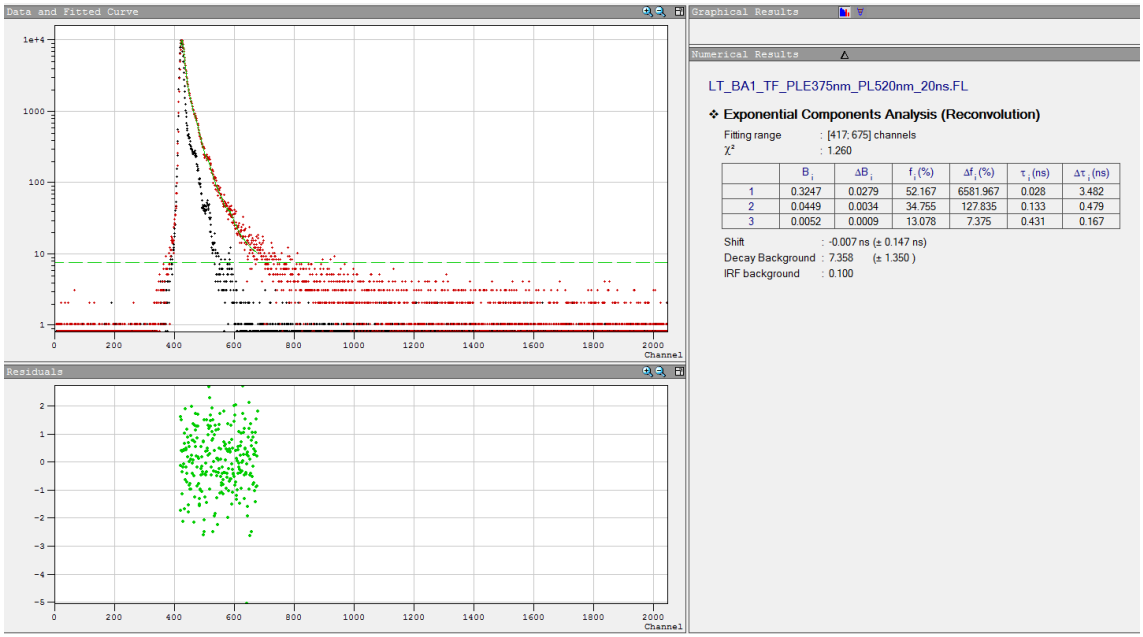

	B_i	ΔB_i	f_i(%)	Δf_i(%)	τ_i(ns)	$\Delta\tau_i$(ns)
1	0.3247	0.0279	52.167	6581.967	0.028	3.482
2	0.0449	0.0034	34.755	127.835	0.133	0.479
3	0.0052	0.0009	13.078	7.375	0.431	0.167

Figure S7. Fit and residual error of the TCSPC decay of the **thin film** of $(BA)_2PbI_4$ with excitation of **375** nm at **520** nm emission.

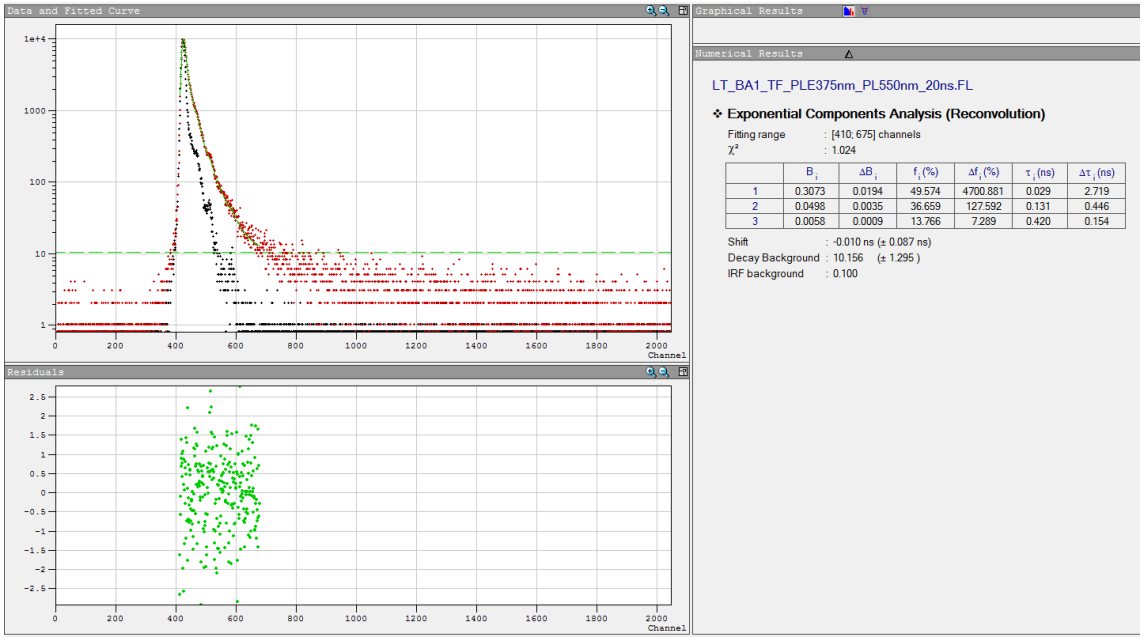

Figure S8. Fit and residual error of the TCSPC decay of the **thin film** of $(BA)_2PbI_4$ with excitation of **375** nm at **550** nm emission.

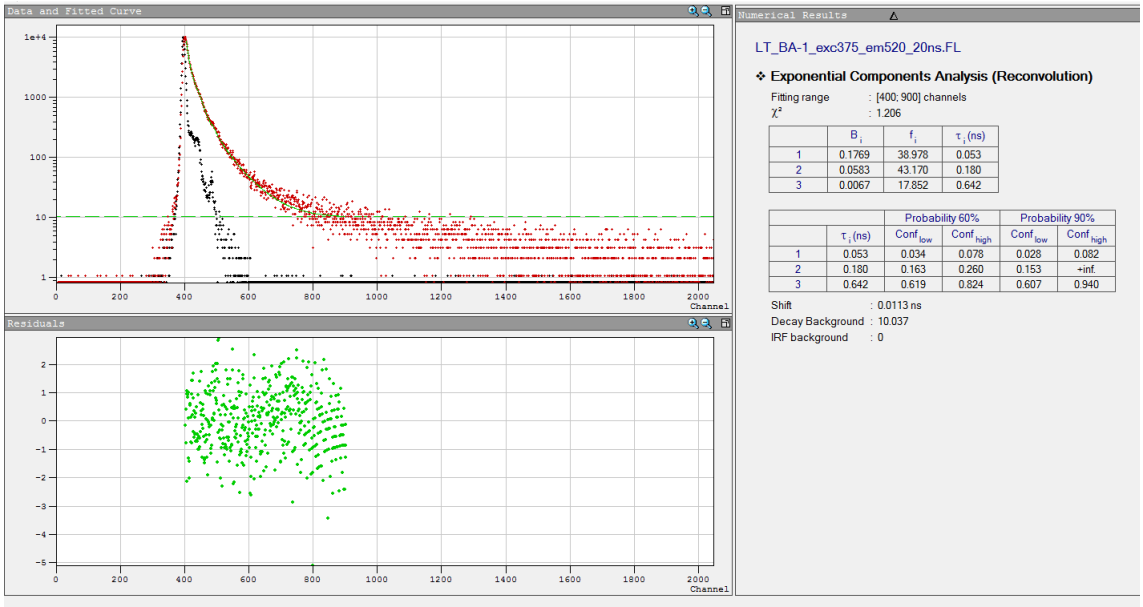

Figure S9. Fit and residual plot of the TCSPC decay of the **powder** $(BA)_2PbI_4$ with excitation of **375** nm at **520** nm emission.

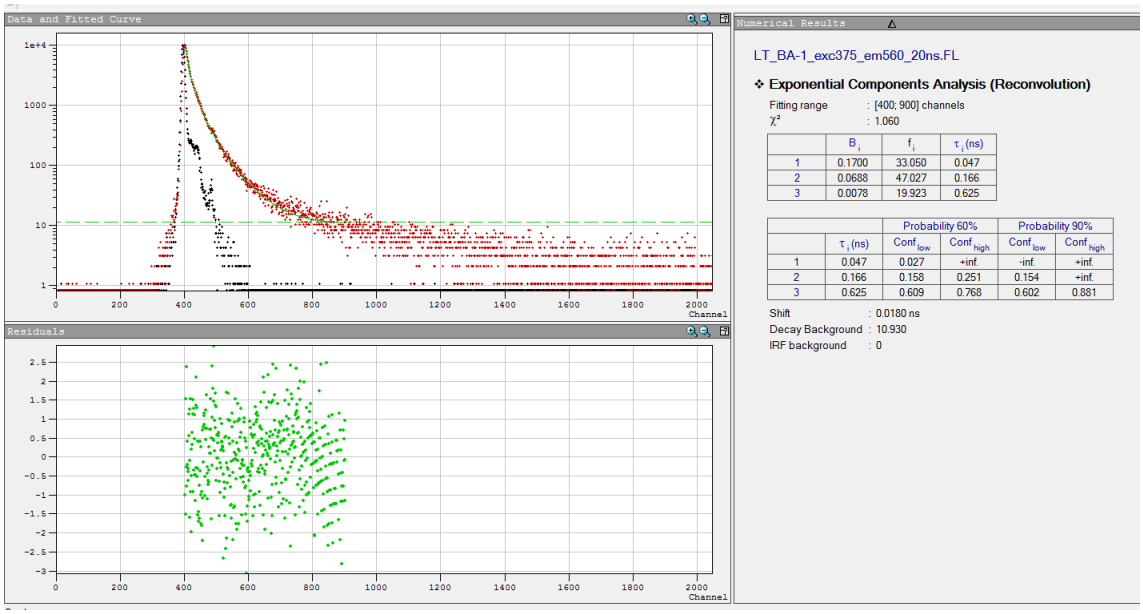

	B_i	f_i	τ_i (ns)
1	0.1700	33.050	0.047
2	0.0688	47.027	0.166
3	0.0078	19.923	0.625

		Probability 60%		Probability 90%	
	τ_i (ns)	$Conf_{low}$	$Conf_{high}$	$Conf_{low}$	$Conf_{high}$
1	0.047	0.027	+inf.	-inf.	+inf.
2	0.166	0.158	0.251	0.154	+inf.
3	0.625	0.609	0.768	0.602	0.881

Figure S10. Fit and residual plot of the TCSPC decay of the **powder** $(BA)_2PbI_4$ with excitation of **375** nm at **560** nm emission.

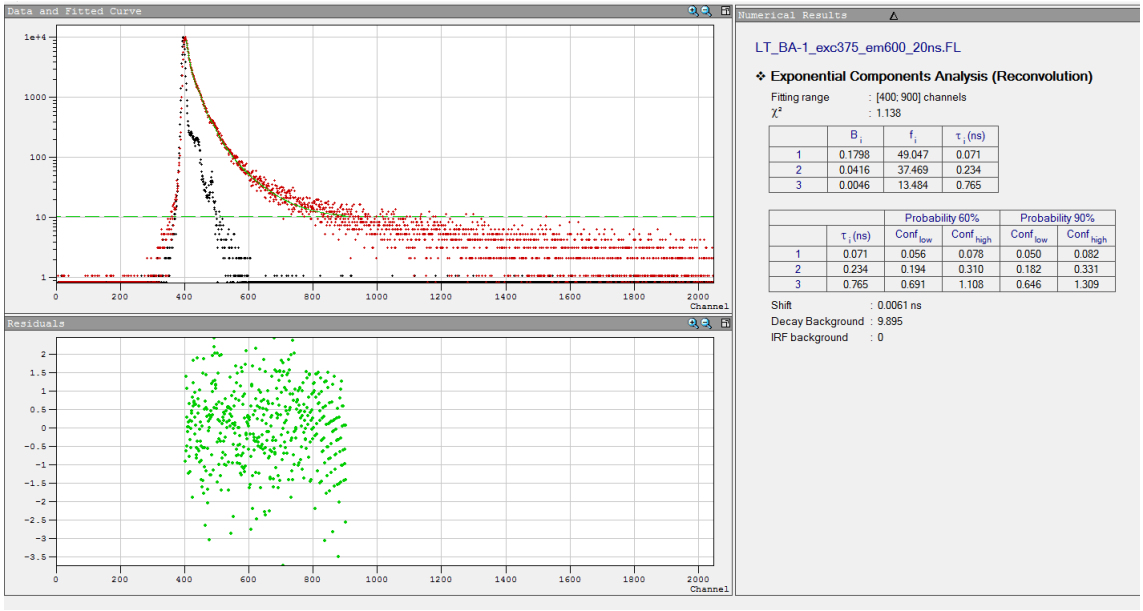

	B_i	f_i	τ_i (ns)
1	0.1798	49.047	0.071
2	0.0416	37.469	0.234
3	0.0046	13.484	0.765

		Probability 60%		Probability 90%	
	τ_i (ns)	$Conf_{low}$	$Conf_{high}$	$Conf_{low}$	$Conf_{high}$
1	0.071	0.056	0.078	0.050	0.082
2	0.234	0.194	0.310	0.182	0.331
3	0.765	0.691	1.108	0.646	1.309

Figure S11. Fit and residual error of the TCSPC decay of the **powder** of $(BA)_2PbI_4$ with excitation of **375** nm at **600** nm emission.

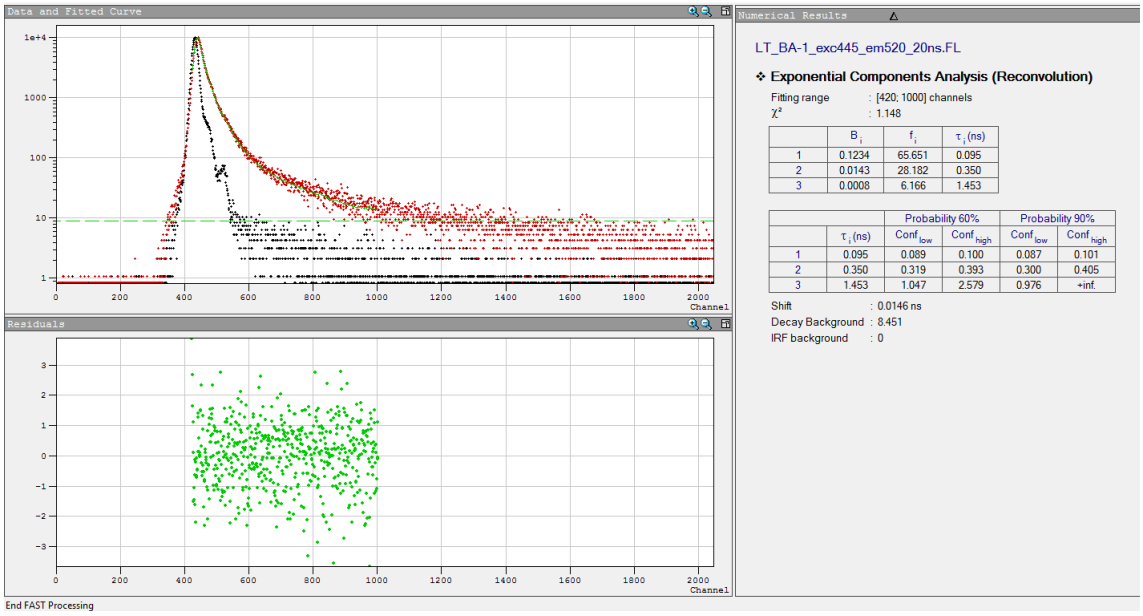

	B_i	f_i	τ_i (ns)
1	0.1234	65.651	0.095
2	0.0143	28.182	0.350
3	0.0008	6.166	1.453

		Probability 60%		Probability 90%	
	τ_i (ns)	$Conf_{low}$	$Conf_{high}$	$Conf_{low}$	$Conf_{high}$
1	0.095	0.089	0.100	0.087	0.101
2	0.350	0.319	0.393	0.300	0.405
3	1.453	1.047	2.579	0.976	+inf.

Figure S12. Fit and residual error of the TCSPC decay of the **powder** of $(BA)_2PbI_4$ with excitation of **445 nm** at **520** nm emission.

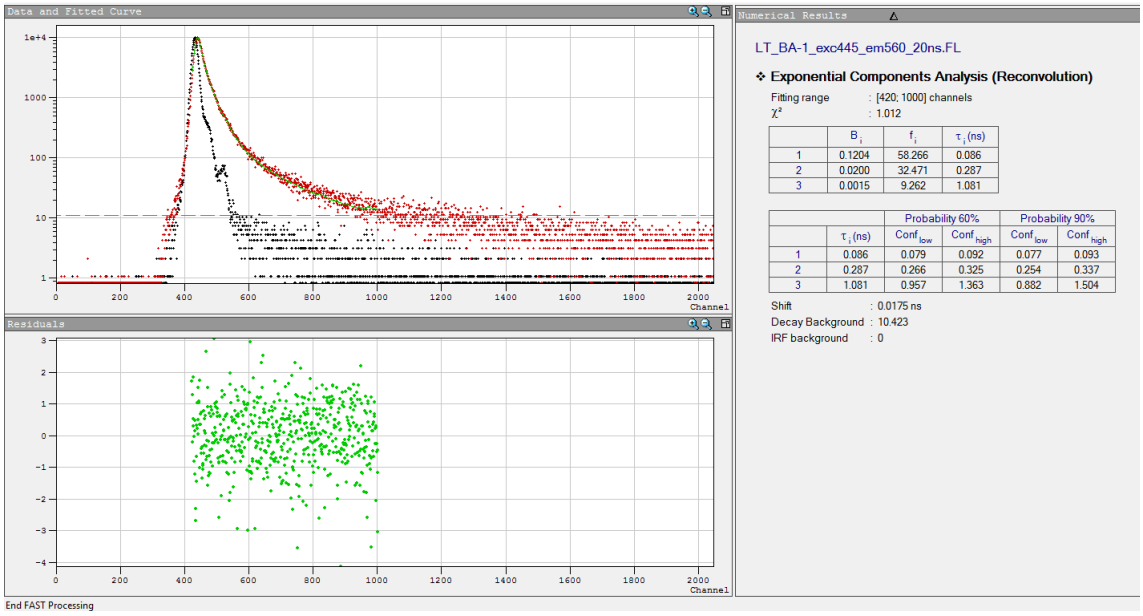

	B_i	f_i	τ_i (ns)
1	0.1204	58.266	0.086
2	0.0200	32.471	0.287
3	0.0015	9.262	1.081

		Probability 60%		Probability 90%	
	τ_i (ns)	$Conf_{low}$	$Conf_{high}$	$Conf_{low}$	$Conf_{high}$
1	0.086	0.079	0.092	0.077	0.093
2	0.287	0.266	0.325	0.254	0.337
3	1.081	0.957	1.363	0.882	1.504

Figure S13. Fit and residual error of the TCSPC decay of the **powder** of $(BA)_2PbI_4$ with excitation of **445 nm** at **560** nm emission.

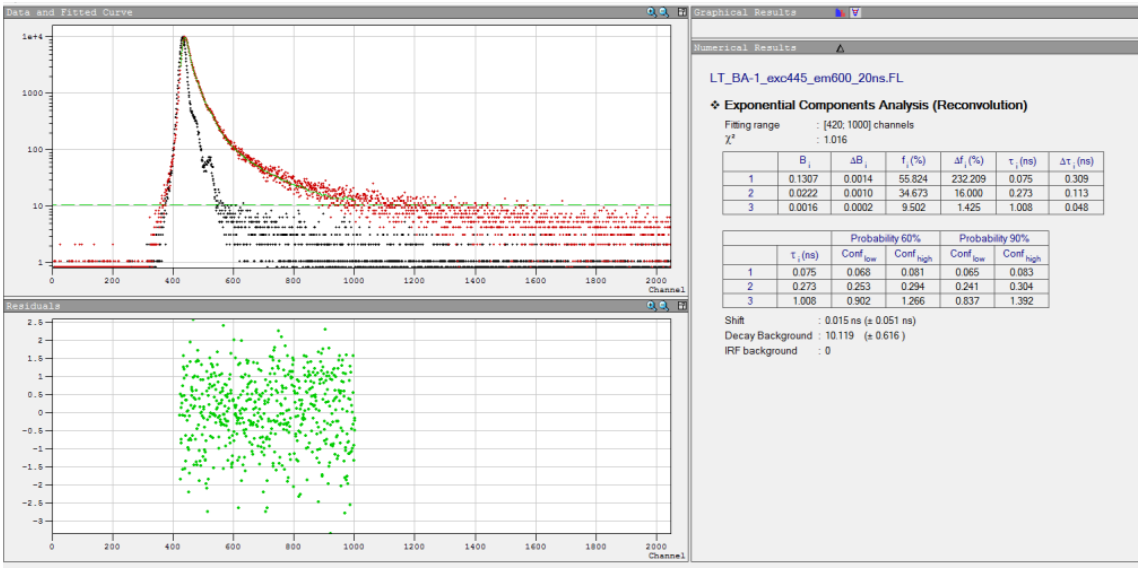

	B_1	ΔB_1	f_1 (%)	Δf_1 (%)	τ_1 (ns)	$\Delta\tau_1$ (ns)
1	0.1307	0.0014	55.824	232.209	0.075	0.309
2	0.0222	0.0010	34.673	16.000	0.273	0.113
3	0.0016	0.0002	9.502	1.425	1.008	0.048

		Probability 60%		Probability 90%	
	τ_1 (ns)	$Conf_{low}$	$Conf_{high}$	$Conf_{low}$	$Conf_{high}$
1	0.075	0.068	0.081	0.065	0.083
2	0.273	0.253	0.294	0.241	0.304
3	1.008	0.902	1.266	0.837	1.392

Figure S14. Fit and residual error of the TCSPC decay of the **powder** of $(BA)_2PbI_4$ with excitation of **445 nm** at **600** nm emission.

Table S1. Parameters taken from the fits of the TCSPC data from the thin film and powder $(BA)_2PbI_4$ (the powder was measured with 2 excitation wavelengths: 375 and 445 nm). The highlight in gray is simply to help visualization.

Sample/Exc. [nm]	Emission [nm]	B_1	τ_1 [ns]	B_2	τ_2 [ns]	B_3	τ_3 [ns]	χ^2
Thin Film 375	520	0.3247	0.028	0.0449	0.133	0.0052	0.431	1.260
Thin Film 375	550	0.3073	0.029	0.0498	0.131	0.0058	0.420	1.024
Powder 375	520	0.1769	0.053	0.0583	0.180	0.0067	0.642	1.206
Powder 375	560	0.1700	0.047	0.0688	0.166	0.0078	0.625	1.060
Powder 375	600	0.1798	0.071	0.0416	0.234	0.0046	0.765	1.138
Powder 445	520	0.1234	0.095	0.0143	0.350	0.0008	1.453	1.148
Powder 445	560	0.1204	0.086	0.0200	0.287	0.0015	1.081	1.012
Powder 445	600	0.1307	0.075	0.0222	0.273	0.0016	1.008	1.016

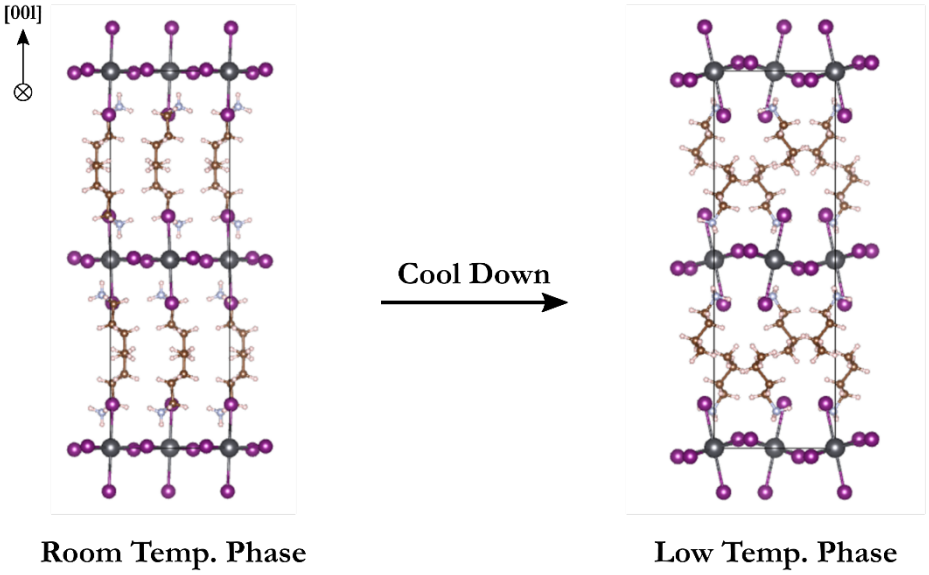

Figure S15. Scheme showing the phase transition of $(BA)_2PbI_4$: both phases are orthorhombic and belong to the same crystalline space group Pbca.

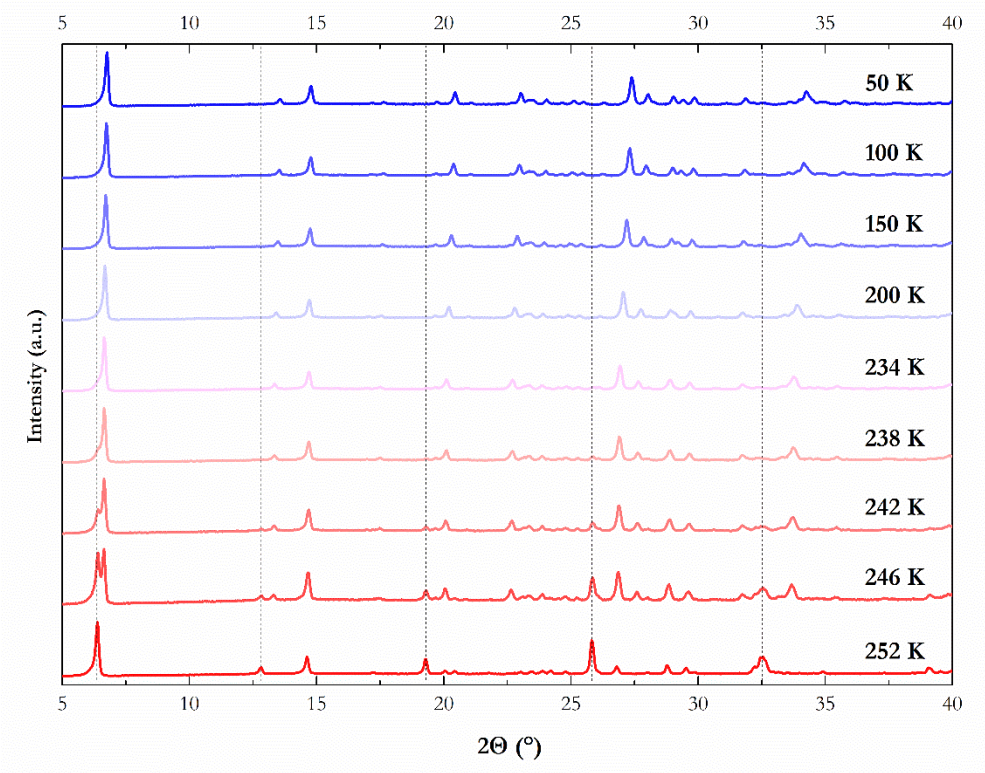

Figure S16. Temperature-dependent powder XRD of $(BA)_2PbI_4$ – dashed lines are simply for visual inspection.

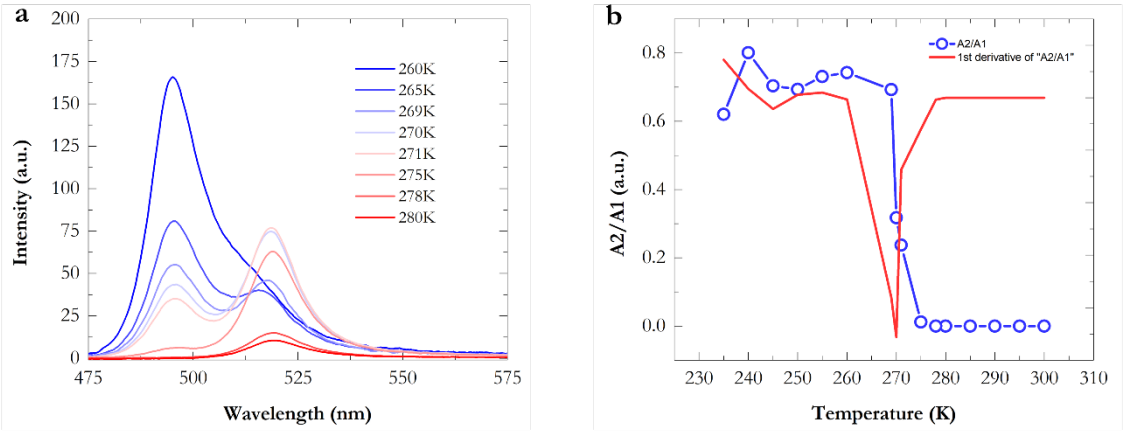

Figure S17. a) Temperature-dependent PL of the thin film of $(BA)_2PbI_2$; **b)** phase transition in the thin film: the blue curve is the ratio between the low-temperature phase and the high-temperature phase (PL peak area); the red curve is the first derivative of the blue curve showing the inflexion at 270 K (the phase transition point).